Int J Appl Earth Obs Geoinformation 84 (2020) 101953

Contents lists available at ScienceDirect

Int J Appl Earth Obs Geoinformation

journal homepage: www.elsevier.com/locate/jag

Peatland subsidence and vegetation cover degradation as impacts of the 2015 El niño event revealed by Sentinel-1A SAR data

Mokhamad Yusup Nur Khakim[a,*], Akhmad Aminuddin Bama[a], Indra Yustian[b], Pradanto Poerwono[a], Takeshi Tsuji[c,d], Toshifumi Matsuoka[e]

[a] Department of Physics, Faculty of Mathematics and Natural Sciences, Sriwijaya University, Indonesia
[b] Department of Biology, Faculty of Mathematics and Natural Sciences, Sriwijaya University, Indonesia
[c] International Institute for Carbon-Neutral Energy Research (WPI-I2CNER), Kyushu University, Japan
[d] Department of Earth Resources Engineering, Kyushu University, Japan
[e] Fukada Geological Institute (FGI), Tokyo, Japan

ARTICLE INFO

Keywords:
Peatland fire
Subsidence
Vegetation cover
Degradation
SBAS
SAR

ABSTRACT

Indonesia has the world's largest tropical peatland, mostly located in the southern province of Sumatra, the south of Kalimantan, and Papua. The catastrophic fires between June and October 2015 induced by the El Niño event burnt most of these peatland areas. We analyzed spatio-temporal peat subsidence during pre- and post-fires in the peat hydrological unit of Sungai Sugihan – Sungai Saleh (KHGSS), South Sumatra using Sentinel-1 images by applying DInSAR-SBAS algorithm. Based on our analysis, the linear subsidence rate after the 2015 peat fires increased by a factor 6.4 compared to that of pre-fires. Generally, the estimated subsidence is temporally well-correlated with the precipitation variation. In addition, the subsidence patterns are spatially correlated with the hotspot distribution, peat thickness, and drainage networks. Furthermore, we mapped vegetation cover over the KHGSS by using the Sentinel-1 images as well. The results show that the vegetation degradation is correlated with the hotspot distribution and the highly-degraded vegetation associated with the 2015 peat fires. It demonstrated that the 2015 El Niño event has significant impacts on increasing the amount of the subsidence and the vegetation degradation in KHGSS area.

1. Introduction

Peatland is one of the wetland ecosystems characterized by the accumulation of organic matter over a long time. Tropical peatlands in Indonesia cover an area of around 20.2 Mha, distributed across Sumatra (7.1 Mha), Kalimantan (5.7 Mha) and the Papua (7.4 Mha) (Murdiyarso et al., 2011). Forested peatlands can mitigate greenhouse gases from the atmosphere. However, this capacity has been threatened by some human activities such as deforesting and draining peatlands, so that the peat becomes dry, oxidized, flammable, and subsidence prone.

The progressive subsidence at drained peatland, due to peat decomposition resulting in CO_2 emission, as well as compaction was schematically illustrated (Hooijer et al., 2010). Total subsidence due to drainage of peat soils includes four components, i.e., consolidation, compaction, shrinkage, and oxidation (Hooijer et al., 2012a,b; Wosten et al., 1997). In addition, the rate of subsidence varies depending on factors such as peat type, rate of decomposition, density and the peat deposit thickness, drainage depth, climate, land use and period of drainage (Grzywna, 2017). Decreasing the water table in tropical peatland makes the peat surface dry and the vegetation dies and becomes fire prone. In the dry season, normally the peat layer can burn to a depth of around 50 cm, but can penetrate to 100 cm in some places (Limin et al., 2008). The fires destroy the peat layers and vegetation; thus, it increases the rate of subsidence (Wosten et al., 1997) . Meanwhile, the fires in degraded peatlands can also quickly release large amounts of the greenhouse gas CO2 (Page et al., 2002).

Between June and October 2015, the peatland in Sumatra and Kalimantan experienced increasingly dry conditions because of a strong El Niño event. Severe fires during the 2015 El Niño-related dry season have burnt large area of these peatlands. As a consequent, vegetation cover and peat surface have been degraded. In addition, the following subsidence increased in the depression of the peatland surface, having the potential to result in the loss of peatland layer. Therefore, peat cannot store water in the pores of its layer, which has experienced severe compaction (Couwenberg and Hooijer, 2013).

The release of carbon dioxide into the atmosphere from the

* Corresponding author at: Jl. Raya Palembang-Prabumulih Km. 32, Indralaya, Ogan Ilir, South Sumatra, 30662, Indonesia.
E-mail address: myusup_nkh@mipa.unsri.ac.id (M.Y.N. Khakim).

https://doi.org/10.1016/j.jag.2019.101953
Received 17 January 2019; Received in revised form 23 August 2019; Accepted 28 August 2019

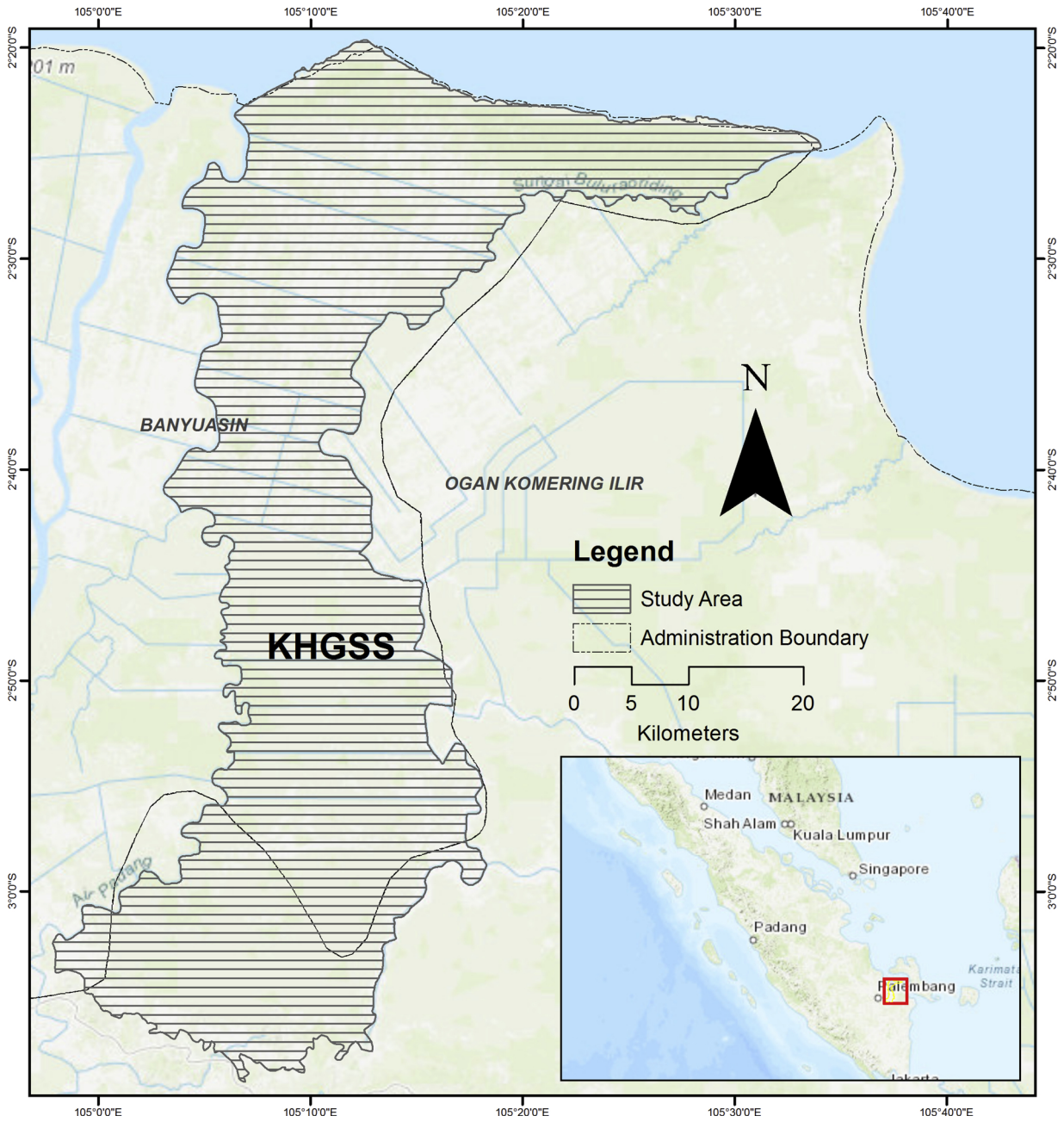

Fig. 1. Location of study area.

oxidation of the soil organic fraction in the upper aerated zone causes a soil mass loss which manifests itself as land subsidence (Gambolati et al., 2005a). This anthropogenic subsidence will increase when the extreme climate events (i.e., hotter and dryer seasons) is longer. The subsidence rate due to bio-oxidation process as the agriculture practices in the Venice peatland was between 1.5 and 2 cm/yr (Gambolati et al., 2005b). Subsidence rates in other sites have also been documented, such as 30 mm/yr in the East Anglian Fenlands, UK (Hotchinson, 1980); 6–50 mm/yr in the Sacramento-San Joaquin Delta, USA (Deverel and Leighton, 2010); 33 mm/yr in Everglade, USA (Stephens, 1956); 75 mm/yr in Johor, Malaysia (Wosten et al., 1997). Cumulative subsidence reported in peat in SE Asia of more than 3 m in thickness over the first 5 years after drainage is between 1 and 1.5 m (Hooijer et al., 2012a,b). Peatland subsidence of 6 m is expected over 100-year drainages, excluding the effect of fires (Page et al., 2002).

The degraded peatland in Central Kalimantan, which was highly drained peatland at around 50 m from canals experienced 0.97 m of total subsidence in 15 years (Hooijer et al., 2014). Oxidation in this area through biological oxidation and fire reached 80% of the total loss of peat volume since drainage, while compaction, i.e., compression above the water table explained 20%. Hooijer et al. (2014) also found that the total amount of subsidence and peat carbon loss is 27% higher in burnt areas compared to areas that are drained but still forested. Furthermore, the burnt and forested high drainage and burnt moderate drainage were estimated to have subsided by 1.08 ± 0.32, 0.86 ± 0.12 and 0.79 ± 0.14 m respectively since drainage in the mid-1990s. From other studies the subsidence rates of peat surface in the Central Kalimantan subsidence based on ALOS SAR images were 7.65 cm/yr with the largest subsidence up to 25 cm from December 2006 to September 2010 (Zhou et al., 2016)

Table 1
The SAR images used in this study.

Subsidence Date acquired* Pre-fire	Bper (m)	Land Cover Date acquired*
20,141,024**	0	20,141,024
20141117	27	20,150,317**
20141211	145	20150504
20150128	74	20150715
20150221	20	20151019
20,150,317	25	20160428
20150410	204	20160802
20150504	−19	20161224
Post-fire		
20,151,112**	0	
20151230	−104	
20160123	−50	
20160311	−41	
20160428	−44	
20160802	−101	
20161013	−52	
20161130	−65	
20161224	−58	

* Dates are in year-month-day format.
** Master Image.

and 2.02 cm/yr from January 2007 to March 2011 (Shimada et al., 2013).

For large, remote, and inaccessible areas, satellite InSAR-based method is powerful for estimating peat subsidence. Our previous studies have successfully applied the InSAR technology using L-band ALOS PALSAR data to estimate land surface deformation (Khakim et al., 2014, 2013). Interferogram coherence of this SAR data is higher than that of C-band Sentinel-1 in vegetated area. However, the L-band data from ALOS 2 is costly and quantitively insufficient for covering the study area. In contrast, C-band Sentinel-1 data is free to access and available with a 12-day repeat cycle in a single pass (ascending or descending).

In this study, we utilized C-band Sentinel-1A dataset to analyze spatio-temporal peat subsidence and vegetation cover changes in the peat hydrological unit of Sungai Sugihan – Sungai Saleh (KHGSS), South Sumatra, Indonesia as a result of the 2015 El Niño event. This study area covers an area of approximately 189,652 ha (Fig. 1). We analyzed the estimated subsidence and vegetation cover changes with corresponding rainfall variation, hotspot distribution, peat thickness, and drainage networks. It must be noted, however, that this study did not separately quantify the peat surface subsidence from each component influencing it, instead of the cumulative impacts.

2. Data and methods

2.1. Hotspot distribution

The VIIRS active fires data (VNP14IMGT) is the latest fire monitoring product to FIRMS (Fire Information for Resource Management System), which identifies global fire locations in near-real time (https://earthdata.nasa.gov/earth-observation-data/near-real-time/firms). Information is collected from the Visible Infrared Imaging Radiometer Suite (VIIRS) sensor. Each dot on the map represents the center of a 375-meter pixel that has been flagged by the algorithm. The VIIRS data replaces the existing fires data from MODIS that was previously available on Global Forest Watch. The VIIRS data has a higher spatial resolution (375-meter pixels vs. 1-kilometer pixels), which improves the detection of smaller fires and provides a more reliable estimate of fire perimeters.

2.2. Subsidence estimation

We used 17 raw (level 1) Sentinel-1A Single Look Complex (SLC) SAR data acquired by the Copernicus Programme satellite constellation conducted by the European Space Agency (ESA). This satellite carries a C-band SAR instrument with a central frequency at 5.405 GHz (Geudtner et al., 2013). Eight SAR data were used to estimate peatland subsidence for the period of before the 2015 peat fire, namely pre-event (24 October 2014 – 4 May 2015) with Path/Frame of 98/1171, while 9 SAR data with Path/Frame of 98/1170 from 12 November 2015 to 24 December 2016 were for after the fire, namely post-event (Table 1). Observation mode is Interferometric Wide (IW) acquired from ascending orbits with single polarization (VV).

ESA's SNAP software was used to perform SAR data processing. For interferometric processing, co-registration of selected SLC images to a single master image was performed with perpendicular baselines less than 204 m. This co-registration ensured that each ground target contributes to the same pixel in both the master and the slave image. We used precise orbits provided by ESA and the Shuttle Radar Topography Mission (SRTM) Digital Elevation Model (DEM) for co-registration, followed by a refinement of the azimuth shift using enhanced spectral diversity (Geudtner et al., 2016; Prats-Iraola et al., 2012). After the co-registration, interferograms were then generated on a burst-by-burst basis.

The level-1 IW SLC product is provided as 3 separate sub-swaths (i.e., IW1, IW2, and IW3) and each sub-swath consists of a series of the bursts. To cover the study area of interest, we concatenated bursts from 1 to 5 and from 3 to 7 of sub-swath IW1 for before and after the 2015 peat fire, respectively. We used the SRTM DEM with the 3-arcsecond resolution to remove topographic fringes. To reduce the phase noises that cause pseudo phase residues and strongly affect phase unwrapping, we applied multilooking and Goldstein phase filtering (Goldstein and Werner, 1998), respectively. Phase unwrapping of the interferogram was conducted using the Statistical-cost, Network-flow Algorithm for Phase Unwrapping (SNAPHU) with a coherence threshold of 0.2 (Chen and Zebker, 2001). After a successful unwrapping process, the interferometric phase images were projected into a map coordinate system (WGS84). These projected interferograms were used for time series analysis based on the Small BAseline Subset (SBAS) method (Berardino et al., 2002; Samsonov et al., 2011).

SBAS retrieves linear deformation rates with corresponding errors and time series of deformation from a set of co-registered unwrapped differential interferograms removing decorrelated areas. We applied high-pass filtering in a spatial domain for each interferogram to remove residual orbital ramps and other long-wavelength noises. Temporal and spatial of atmospheric disturbances produce an offset in each interferogram. The atmospheric phase delay can be estimated by a generic InSAR atmospheric correction model (Yu et al., 2018a, 2018b). This model has been developed by using both HRES-ECMWF grid model output and GPS ZTD pointwise observations, tightly integrated using the ITD model to produce atmospheric correction maps.

A simultaneous inversion was performed by applying singular value decomposition (SVD) to estimate deformation rates and residual topographic errors (Samsonov et al., 2011). The linear deformation rates were then calculated using the linear regression algorithm. The errors of the linear deformation rate were also calculated. Furthermore, the cumulative deformations were reconstructed by integration (Kwoun et al., 2006).

2.3. Land Cover mapping and change detection

Land cover was obtained from eight level-1 Sentinel-1A IW SLC SAR images with variable rainfall (Table 1). All of the images used are in VV polarization mode. SAR data pre-processing of the Level-1 SLC image was performed using the SNAP software including calibration, thermal noise

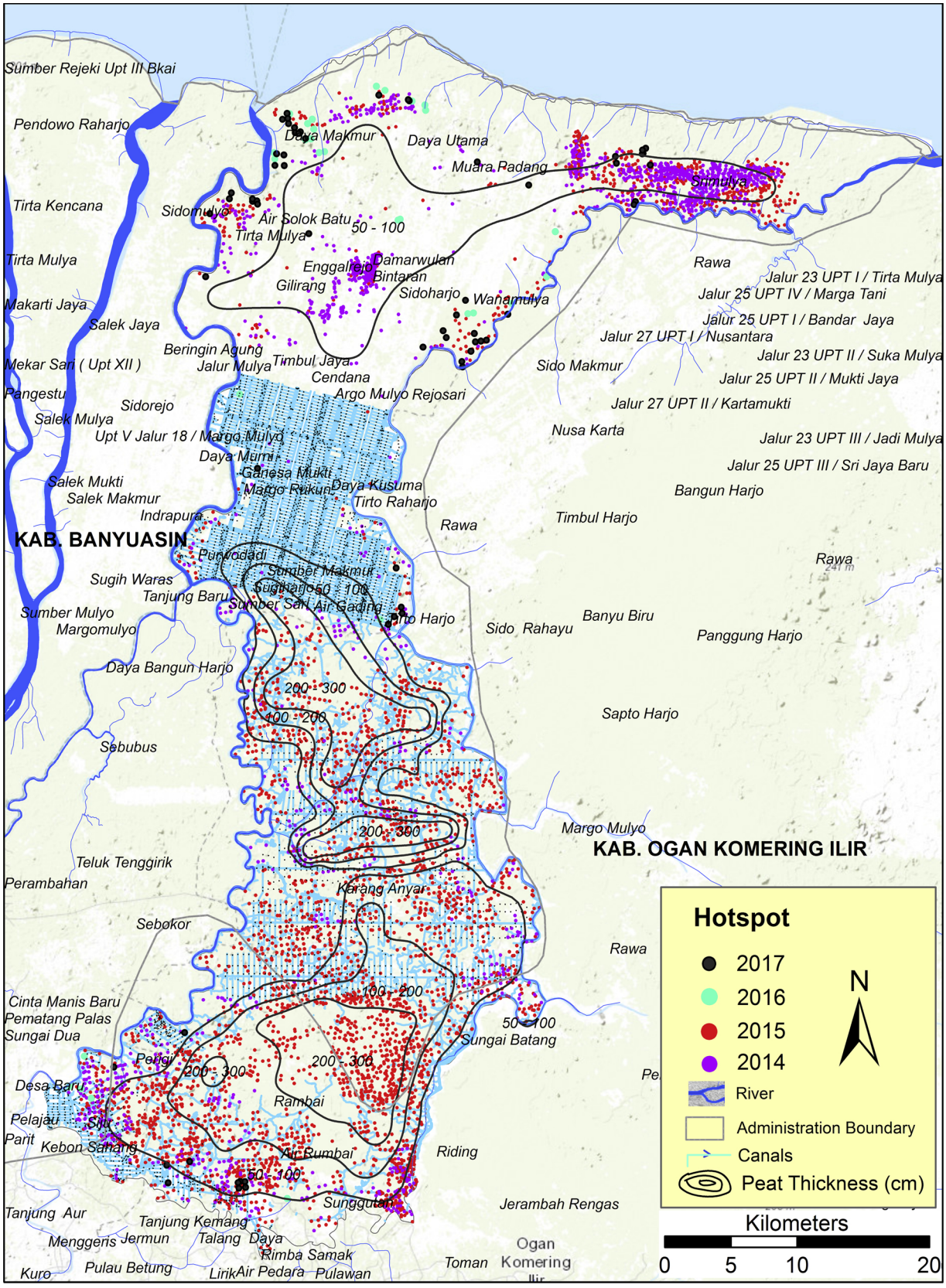

Fig. 2. Hotspot distribution, canal networks, and peat thickness in the KHGSS.

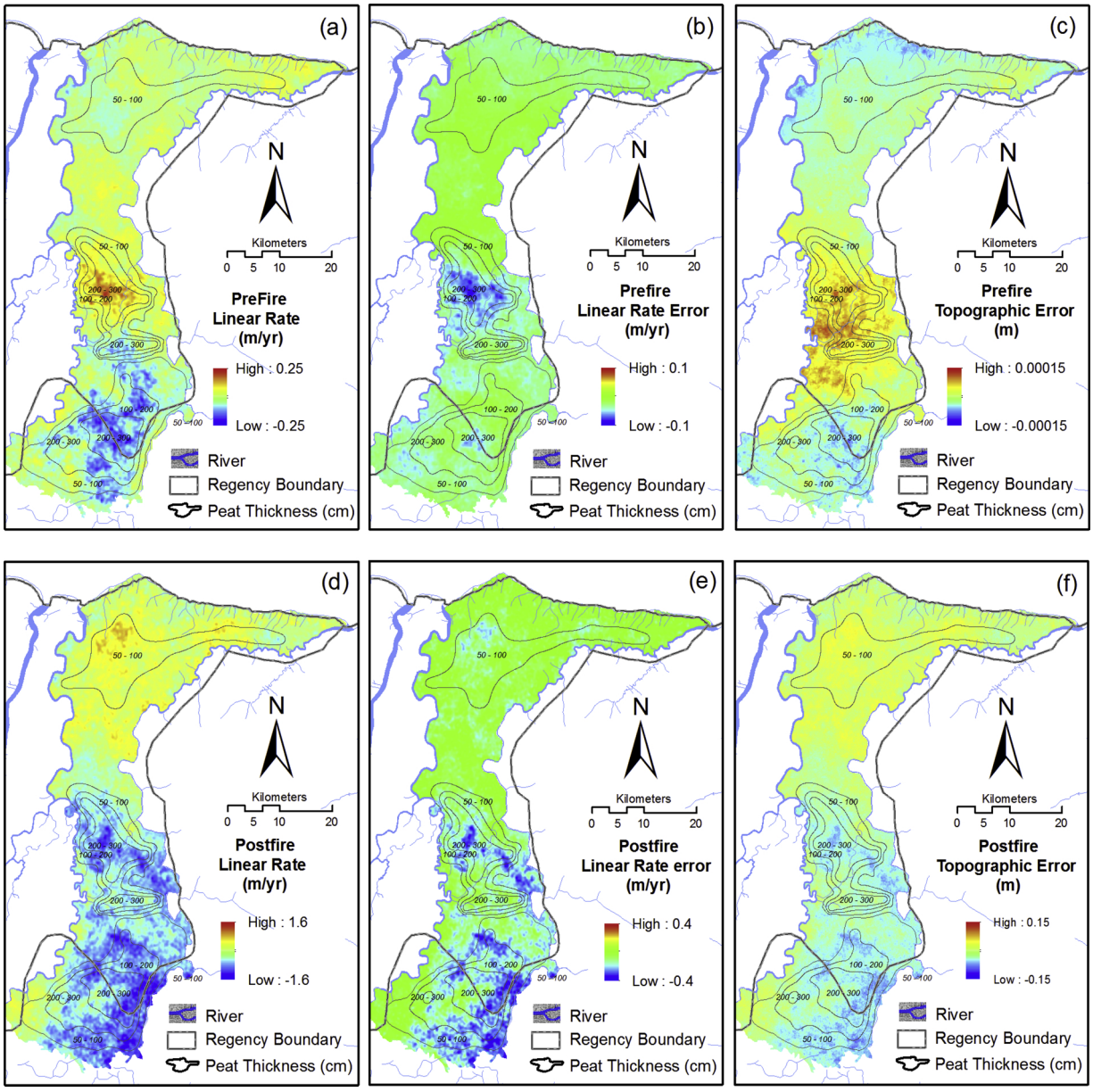

Fig. 3. Linear rate, linear rate error, and topographic error for pre- and post-fire 2015.

removal, TOPSAR deburst, mosaicking, as well as 4 × 4 multilooking. Speckle effects, which are characteristic of radar images influencing the radiometric information, were compensated using a Refined Lee low-pass filter, which averages the images while preserving feature edges (Wang et al., 2012). Thus, these images were converted to the backscatter coefficient (σ^0) values in the decibel unit (dB), terrain corrected using SRTM DEM, and geocoded to map projection (WGS84) before classification.

Land cover was classified using unsupervised K-means cluster analysis in the SNAP toolbox. The classification was performed with 30 iterations to produce four major land cover classes, i.e., forest/plantation, shrub/bush, cultivation/bare land, and water. A confusion matrix was used to calculate the frequency of class agreement between reference ground truth data and SAR-based classified land cover map. Accuracy measures of land cover classification are user's and producer's accuracy, error commission and omission, overall accuracy, and Kappa coefficient. A spatial change map was obtained by subtracting the land cover of 2015/03/17 (as a baseline) from those of other dates for the same area.

3. Results and discussion

The extreme climate due to the 2015 El Niño caused an increase in vulnerability of peatlands in this area from surface subsidence and vegetation degradation. To investigate these impacts, we used hotspots obtained from the Visible Infrared Imaging Radiometer Suite (VIIRS) active fires data and a canal map derived from LiDAR data (BRG, 2017). The hotspot distribution for the period from 2014 to 2017 shows that the most severe fire occurred in 2015 (Fig. 2). Most hotspots occurred in the southern part of the study area dominated by peat layers with the thickness in a range of 50–300 cm.

3.1. Peat surface subsidence

Peat surface displacements were estimated for two periods (pre- and post-event) to evaluate impacts of the extreme climate due to the 2015 El Niño event on spatio-temporal subsidence in the KHGSS area. The maps of linear deformation rates and errors are presented in Fig. 3**A–B and d–e** for pre- and post-events, respectively. The rate of

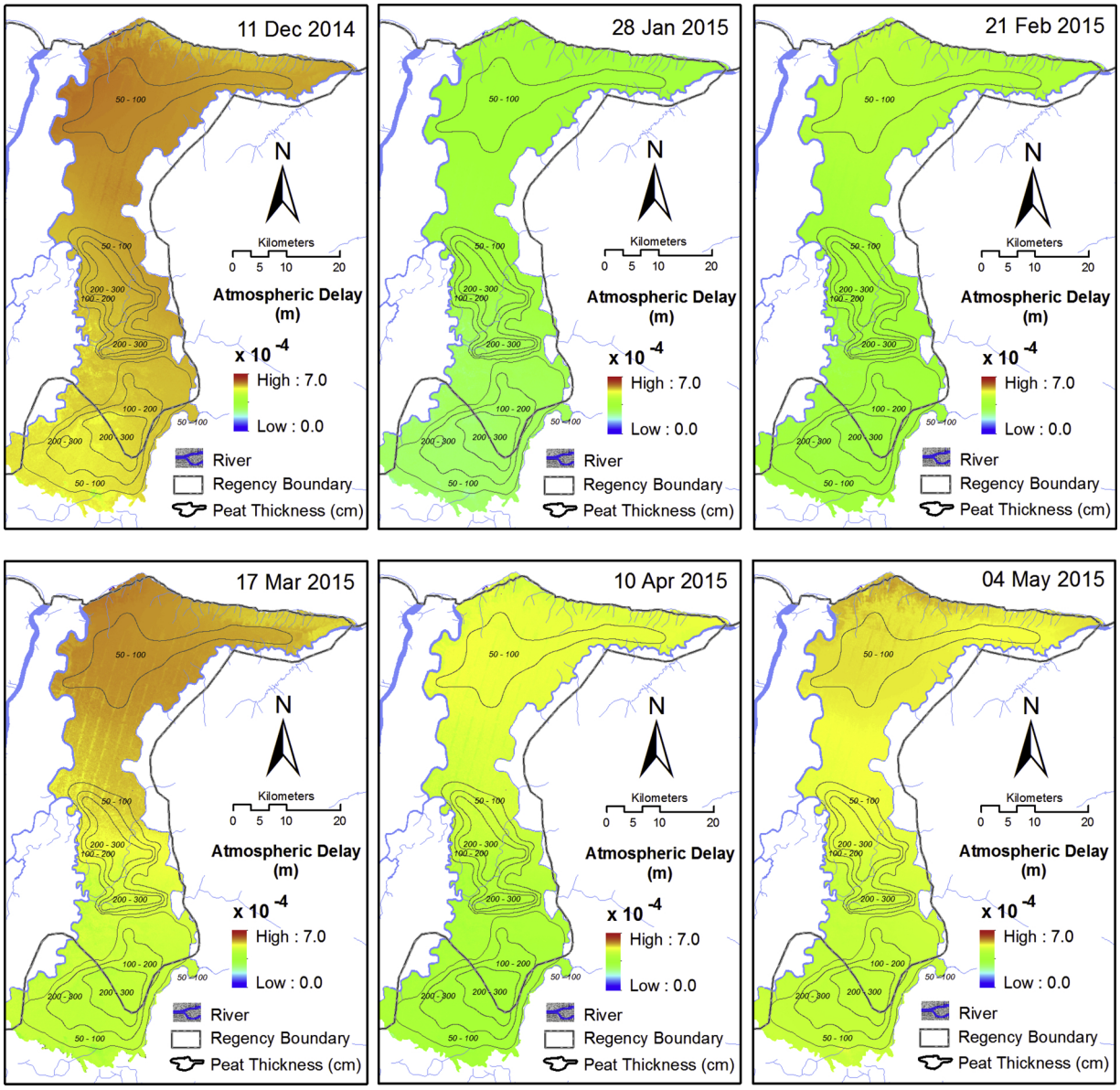

Fig. 4. Spatio-temporal atmospheric path delay for pre-fire 2015.

this linear subsidence for pre-event increased by a factor 6.4 compared to that of the pre-event. Furthermore, estimate topographic errors are ± 1.5E-04 m for pre-events (Fig. 3c) and ± 1.5E-01 m for post-events (Fig. 3f), respectively. Moreover, spatiotemporal atmospheric delays estimated based on a generic InSAR atmospheric correction model are only up to ~7.0E-04 m (Figs. 4 and 5). Thus, atmospheric disturbances insignificantly affected the deformation.

Subsidence generally occurred in the southern part of the study area, namely Karang Anyar and Rambai village, spatially associated with peat areas (Fig. 6). We compared subsidence rates to the distribution of fire hotspots. Subsidence during the pre-event is spatially uncorrelated with the 2014 hotspot distribution but correlated with the peat thickness. The 2014 fire hotspots were generally distributed along the edge of the peatland area, burning being the cheapest and most comfortable means of site preparation for cultivation and plantation. Peat surface subsidence is controlled by drainage and water levels during pre-events. This lowering water level also increased the peat compaction and oxidation above the water table. Furthermore, the consolidation may also increase below the water table.

It can also be shown that dense artificial canals have been extensively established at or around the subsiding area. Moreover, these subsiding areas are also located near the river, which fast discharged much amount of water from peatland. There are several components associated with drainage inducing subsidence in peatlands such as oxidation, compaction and shrinkage, and consolidation (Hooijer et al., 2012a,b). These components increased in subsidence magnitude when groundwater is removed by dense drainage canals. The oxidation decomposed peat in the aerated zone above the water table. Compaction reduced peat volume in the aerated zone above the water table resulting from the pressure applied on the peat surface by heavy materials and shrinkage occurs through contraction of organic fiber when drying. Meanwhile, consolidation compressed saturated peat below the water table due to loss of buoyancy of the top peat.

In contrary, post-fires subsidence patterns are spatially-well correlated with the 2015 hotspot distribution, which mostly occurred in the peat areas (Fig.7). From subsidence map, the area around point 1 (▲[1]) located in Northern Karang Anyar did not subside during pre-fire 2015. Despite no artificial canal networks established in this area, significant

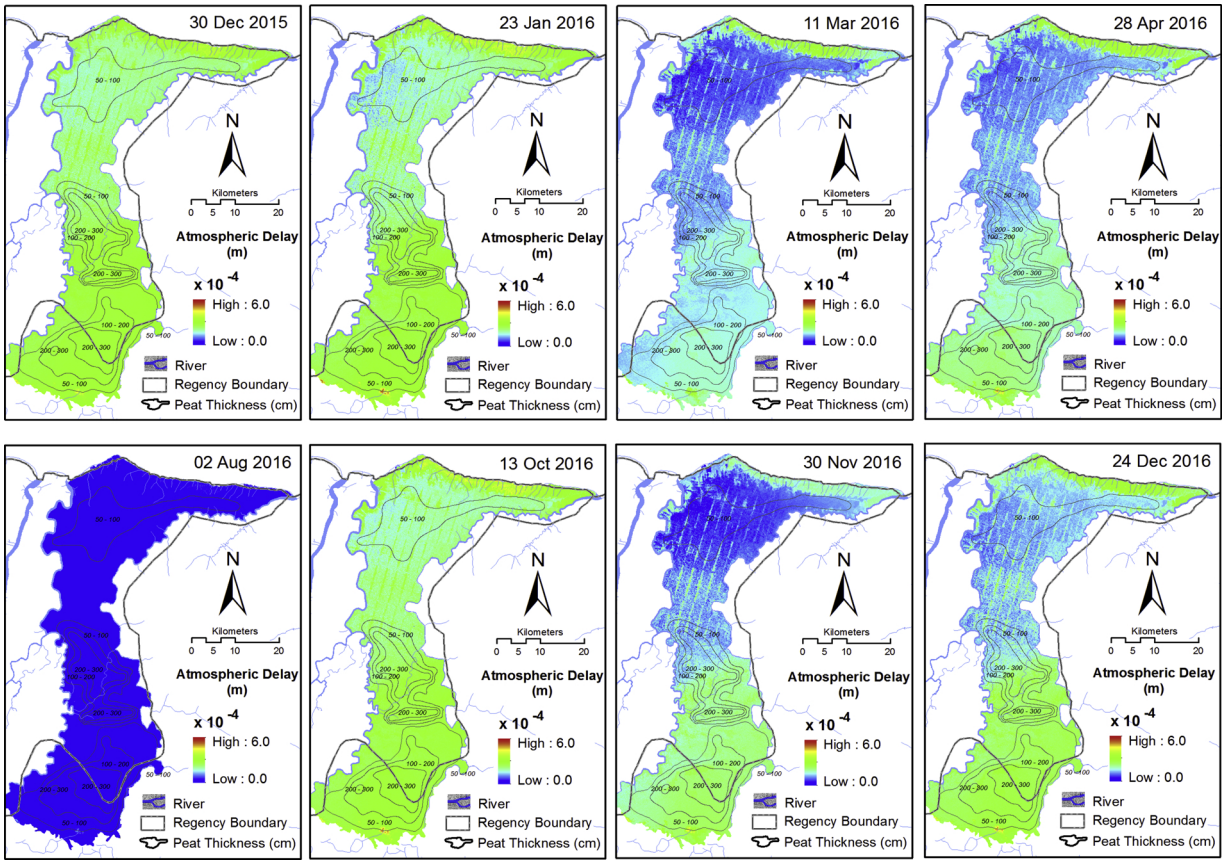

Fig. 5. Spatio-temporal atmospheric path delay for post-fire 2015.

subsidence was observed after the 2015 peat fires. A significant decrease in rainfall during the 2015 extreme El Niño event caused the peat surface dry, the vegetation dies and becomes fire prone. In the dry season, usually, the peat layer can burn to several depth and fires can penetrate to 100 cm in some places (Limin et al., 2008). The combustion of the peat layer present at several depths also led to the creation of subsurface hollows at different places (Roy et al., 2014). Thus, the volume reduction associated with the peat burning likely caused the subsidence in this area. Subsidence also increased due to peat fires in several areas, especially around the points 2–6 (▲$^{2-6}$) located in Southern Karang Anyar, Rambai, and Rumbai. In these areas, an amount of subsidence during this period became much larger than that of the pre-fires. Subsidence magnitude estimated from the SBAS-DInSAR technique reached ~0.12 m and ~2.5 m during the pre- and post fires of 2015, respectively.

Furthermore, we constructed 14 time-lapse profiles of subsidence across the center of the peat dome along lines A–B and C–D (Fig. 8a). These profiles indicate that more considerable subsidence occurred in areas which are closer to the river discharging water from peatland. These areas also experienced severe fires during the 2015 extreme El Niño drought.

Estimated trends of nonlinear subsidence may correspond with the water level. Information of the water level during study periods in the KHGSS was unavailable; we thus compared the deformation of surface peatland at seven locations to rainfall variation for seasonal analysis of subsidence characteristics during the study period (Fig. 8b). The trends of peatland subsidence are generally correlated with the rainfall variation. However, the first six months after the 2015 peat fires, the subsidence trends do not correlate with rainfalls suggesting the precipitation during these months did not penetrate the peat pores after the severe fires.

3.2. Land cover changes

Spatio-temporal land cover was classified based on Sentinel-1 data with single polarization (VV) using unsupervised K-means cluster analysis. The previous study shows that VV has higher accuracy than VH for the land cover classification (Abdikan et al., 2016). The classification was performed with 30 iterations to produce 4 major landcover classes, i.e., forest/plantation, shrub/bush, cultivation/bare land, and water. Fig. 9 shows examples of different land cover classes. Tall woody vegetations such as palm plantation, rubber plantation, secondary and primary forests are grouped into a forest/plantation class. Meanwhile, lower vegetations such as shrub, bush, and grass are merged as a shrub/bush class; rice field, cultivated area, degraded area, and bare land are merged as a cultivation/bare land class. In addition, water class is used to identify fish pond, river, and other water bodies.

We evaluated the accuracy of land cover classification using ground truth data because optical data, such as both Sentinel-2 and Landsat 8, covering the study area are heavily cloudy/hazy during study periods. Locations of these ground truth surveys are presented in Fig. 9. The accuracy assessments (Conglaton, 1991; Story and Congalton, 1986) including User's Accuracy (UA), Producer's Accuracy (PA), Error Commission (EC), Error Omission (EO), Overall Accuracy (OA), and Kappa are presented in Table 2. The overall accuracy and Kappa of classification is 91% and 84%, respectively. The accuracy of the water class is the highest for both the user's and producer's accuracies in the land cover classification. On the other hand, the lowest user's and producer's accuracies are respectively cultivation/bare land and shrub/bush classes.

The land covers were mapped for the period 24 October 2014 to 24 December 2016 (Fig.10). Since the peat fires have been suspected of contributing to vegetation cover degradation, we have overlain the

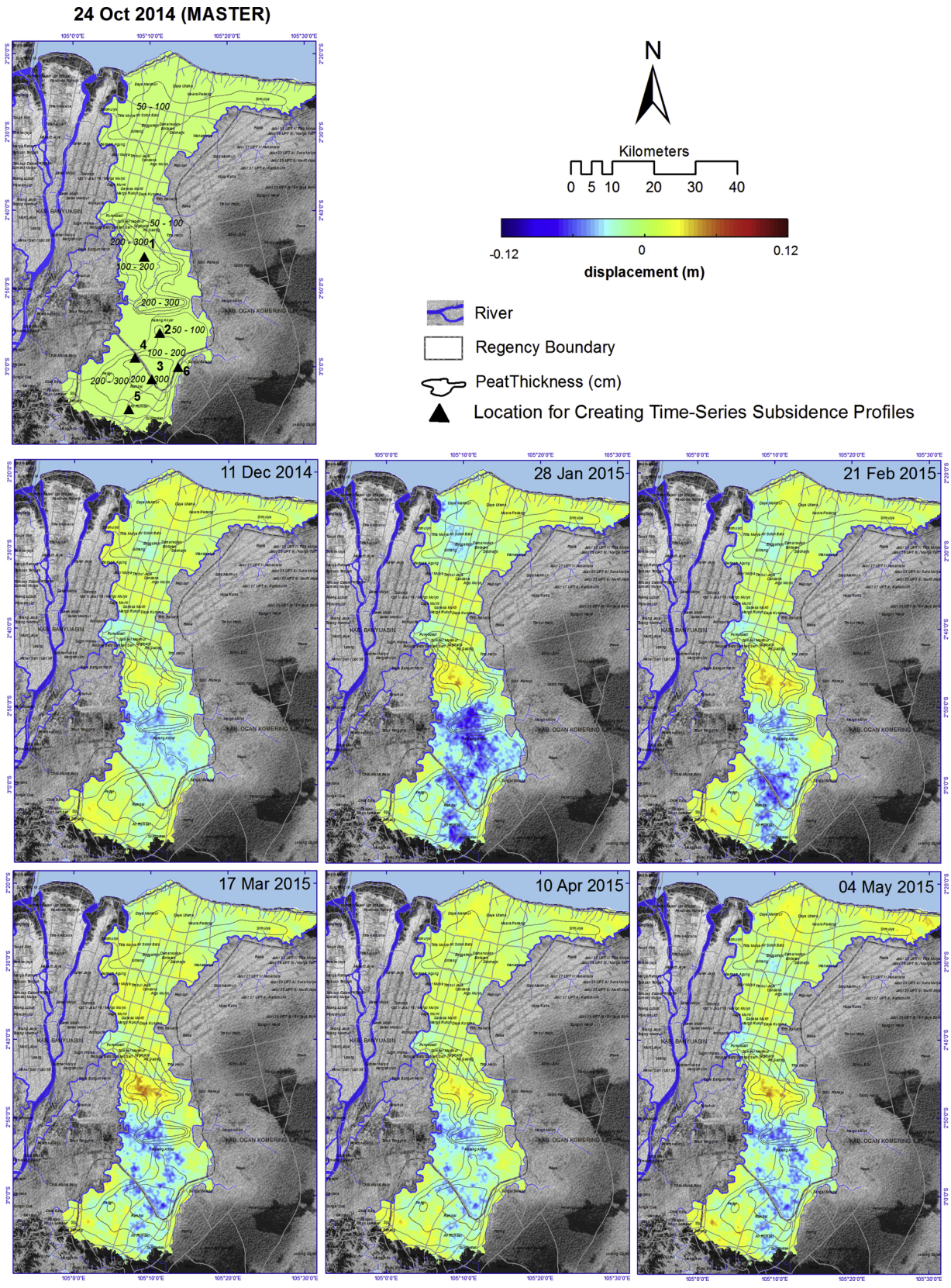

Fig. 6. Sequential subsidence patterns in the KHGSS for prefire 2015.

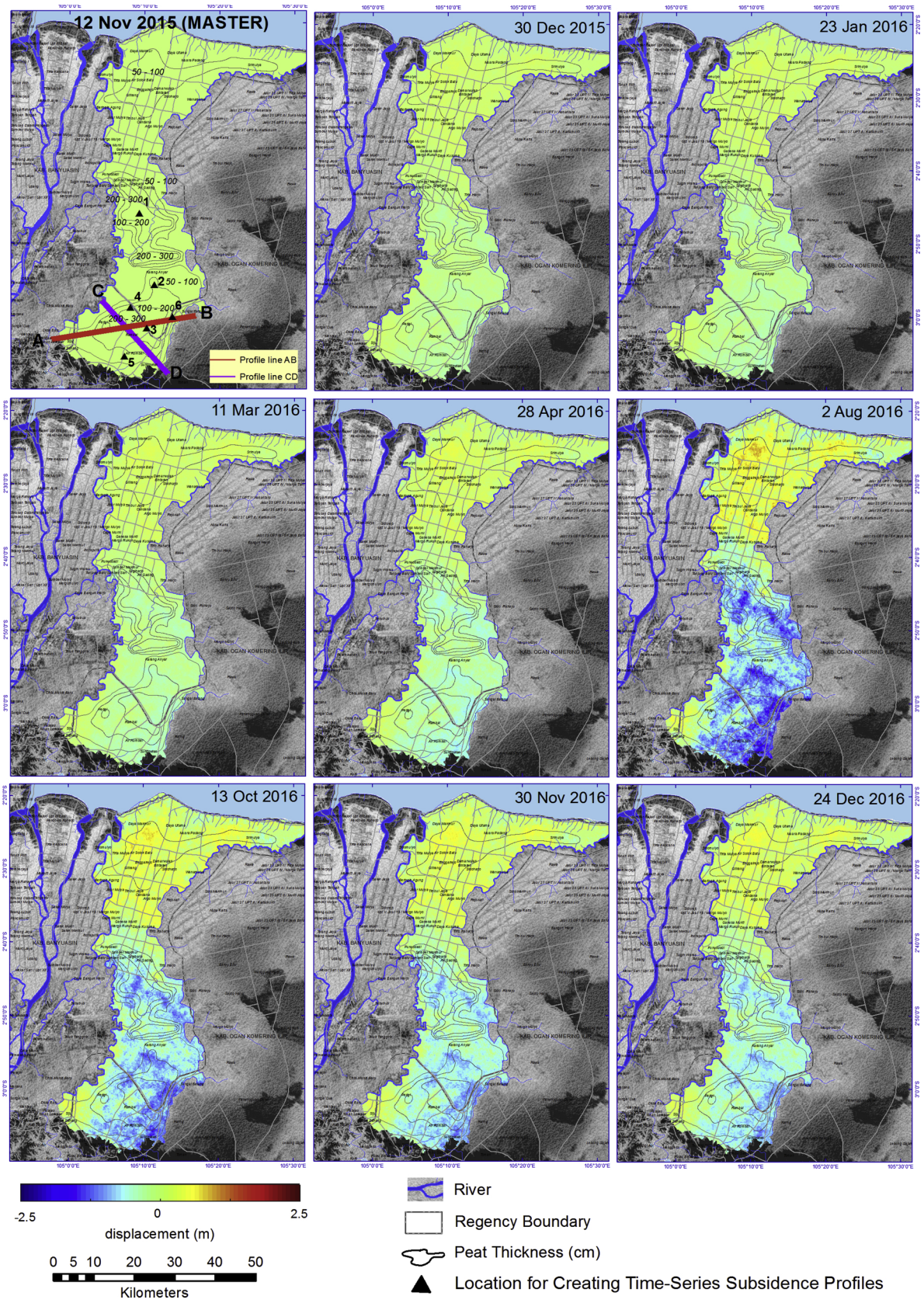

Fig. 7. Sequential subsidence patterns in the KHGSS for postfire 2015.

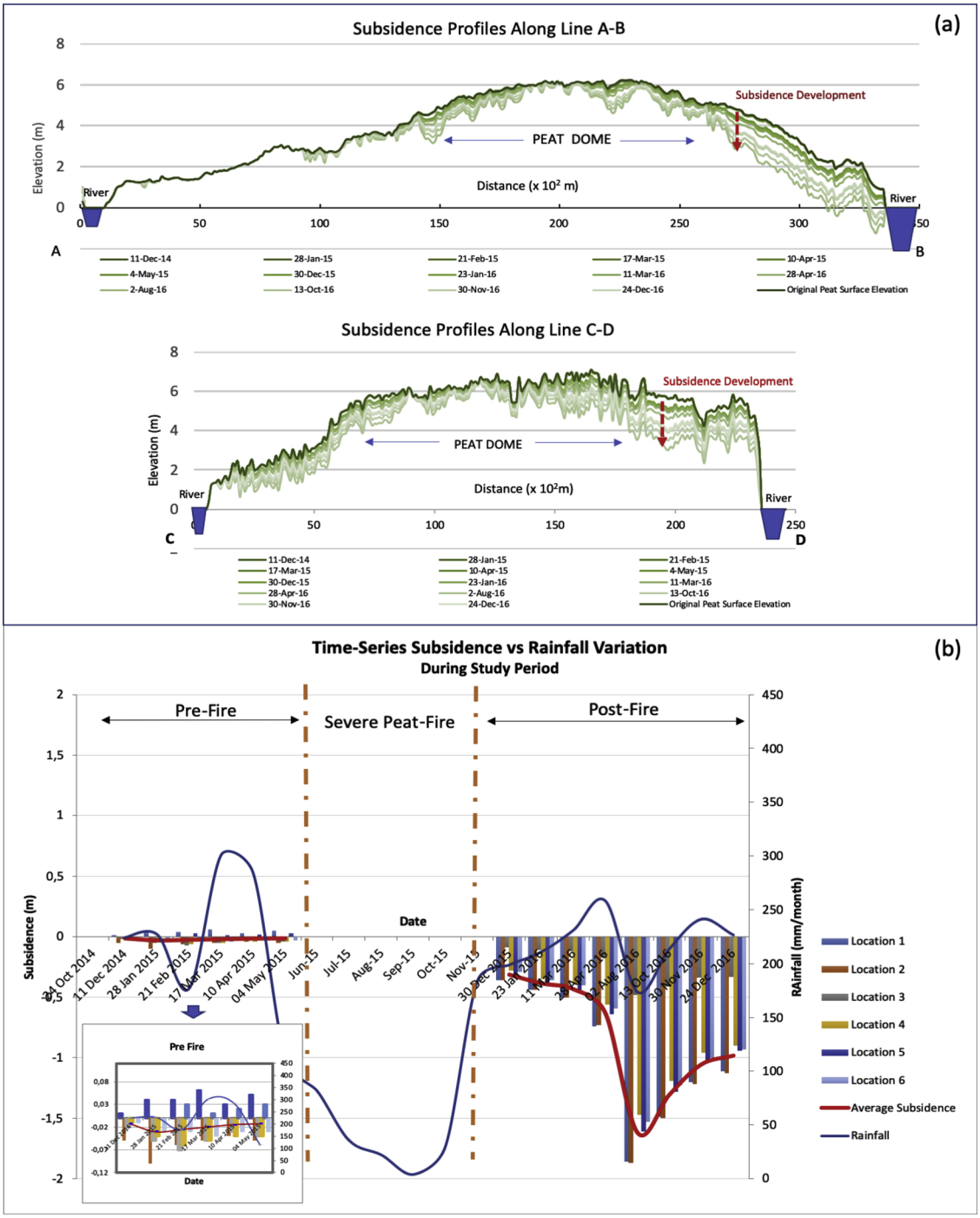

Fig. 8. (a) Profiles of subsidence along lines A–B and C–D (Fig. 7) crossing peat dome and (b) Comparison between peat surface subsidence trends for six selected locations and rainfall variation.

classified land cover with monthly hotspot distribution. Generally, the degradation of land cover is spatially associated with the distribution of fire hotspots. The gradation is indicated with the change in land covers from vegetated areas (dark/light green) into bare land (orange). Most fires in 2014 were associated with land preparation for cultivation and plantation. However, high degradation occurred when mainly dry period from July to October 2015, a result of the 2015 El Niño, contributed to a severe fire season (Fig. 10e).

Furthermore, the classified land cover maps for different time are also analyzed qualitatively by calculating spatial change map. For this calculation, the cultivation/bare land and water classes were merged to bare land class each land cover map. Estimated change maps are presented in Fig.11. Light degradation is used to show the change in vegetation cover from forest/plantation class to shrub/bush class or from shrub/bush class to bare land class; high degradation is the change from forest/plantation class to bare land class. From the change maps, highly degraded areas are generally related to land fire locations. On the other hand, lightly degraded/growth areas are seemly related to a seasonal change.

The change in land cover is also quantitatively analyzed by calculating the percentage of land cover areas and their changes (Fig.12).

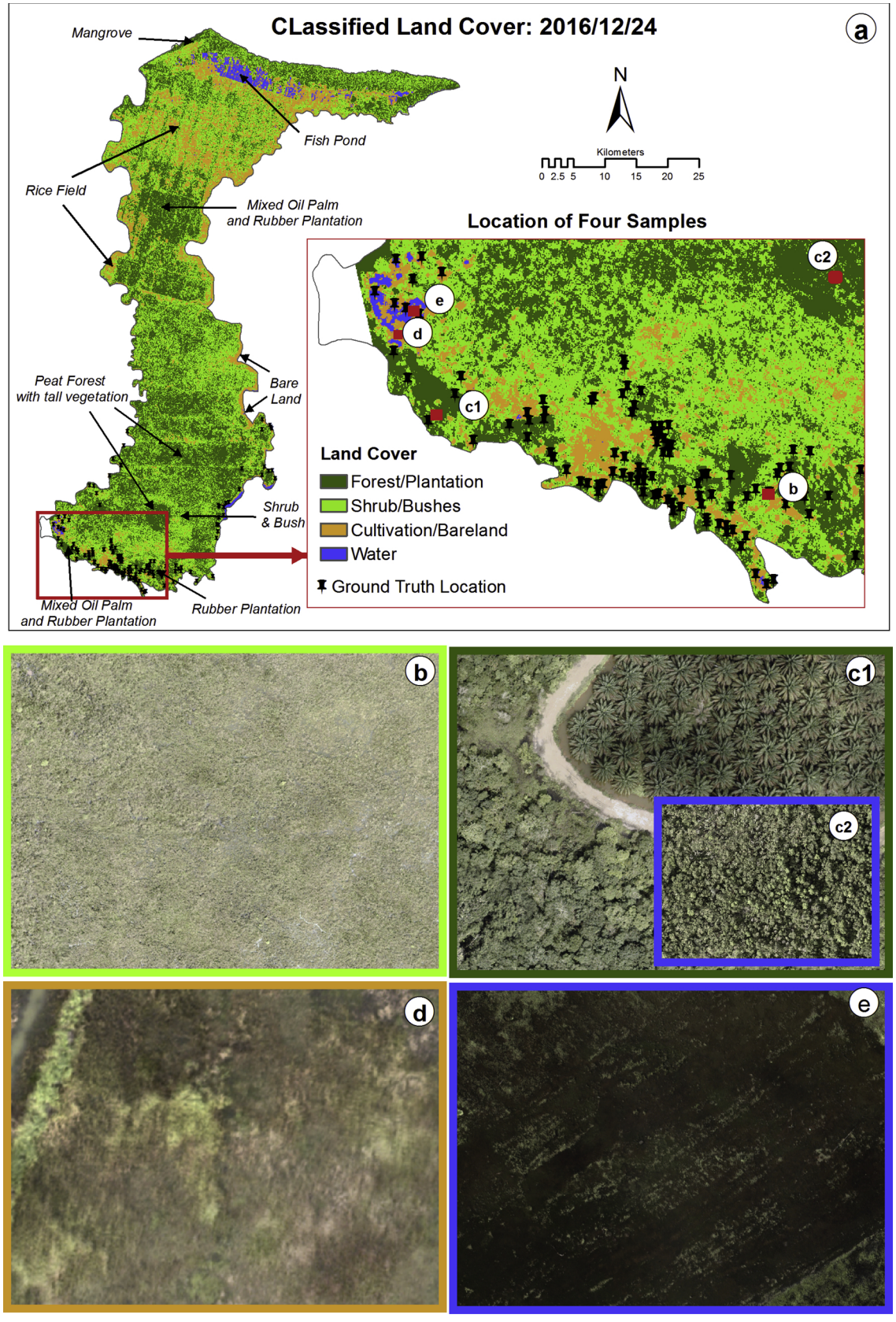

Fig. 9. (a) Description of classified land cover image of 24 December 2016 and ground truth locations; aerial photographs for 4 classes in the KHGSS; (b) shrub/bush; (c1) oil palm and rubber and (c2) peat forest vegetation; (d) bare land; and (e) water.

Table 2
Measures of accuracy assessments for land cover classification.

No	Classes	UA	PA	EC	EO	OA	Kappa
1	Shrub	88%	88%	12%	12%	91%	84%
2	Forest/Plantation	95%	90%	5%	10%		
3	Cultivation/Open Land	79%	96%	21%	4%		
4	Water	100%	100%	0%	0%		

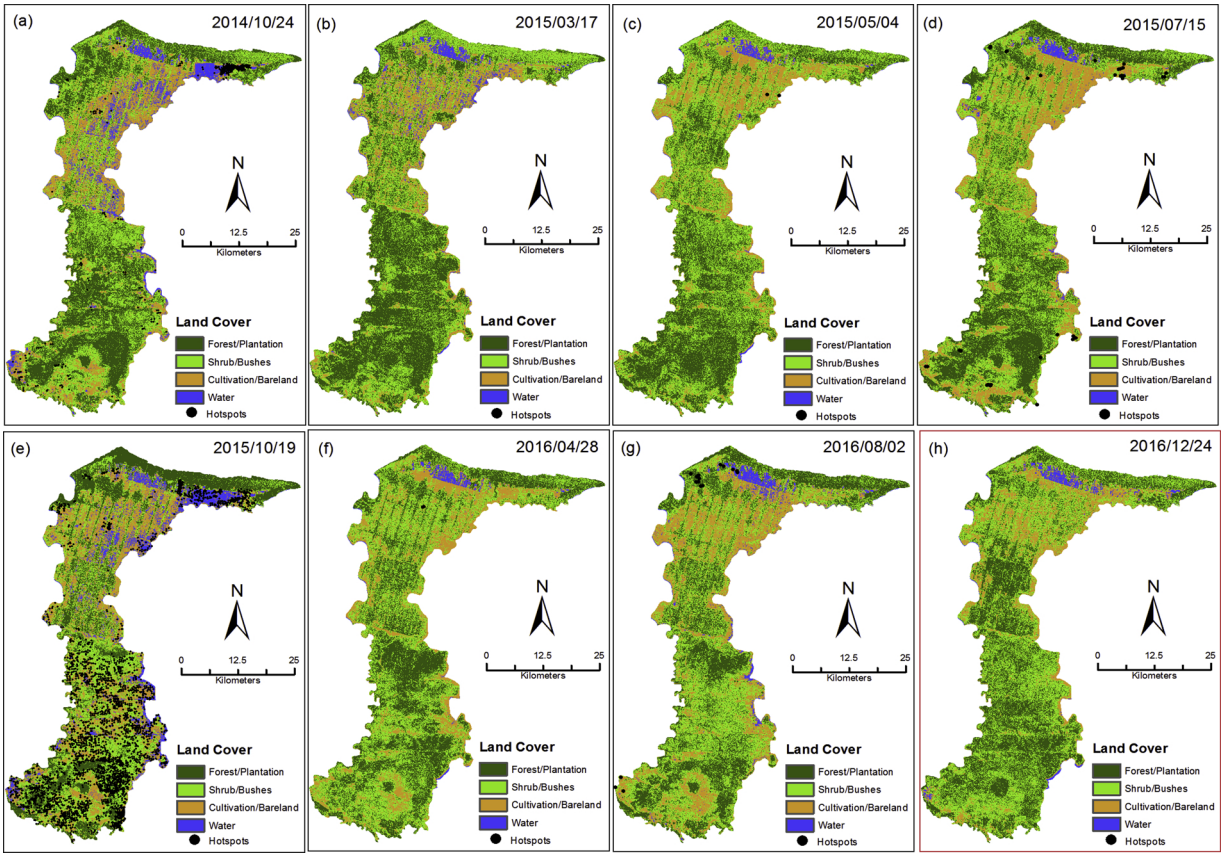

Fig. 10. Classified land cover maps overlaid with corresponding monthly hotspots from 24 October 2014 to 24 December 2016.

The forest/plantation class has the most significant decline compared with other classes during the study period, especially in October 2015. In this time, the degradation of vegetation cover is the highest, 41%. However, there was a trend of vegetation re-growth for post-fire. This post-fire vegetation re-growth indicates the potential of vegetation succession for carbon storage and regeneration.

4. Conclusion

Spatio-temporal peatland subsidence and vegetation cover have been successfully mapped based on Sentinel-1A C-band SAR data using SBAS-DInSAR technique and K-means classification, respectively. The results indicate that peat surface subsidence was caused by drainage, which might increase consolidation, oxidation, and shrinkage of peatland during pre-fire 2015. The subsidence spatially occurred in areas which are with denser drainage canals and closer to the river draining the peatland. The subsidence rate was as much as ~0.25 m/yr for the pre-fire period.

On the other hand, the linear rates of peat surface subsidence highly increased by a factor 6.4 after the 2015 fires related to the El Niño drought. The estimated trends of subsidence are temporally well correlated with rainfall variation. Significant decrease in the rainfall during this period is mainly inferred decreasing the peat water levels and therefore more considerable subsidence occurred. Besides consolidation, oxidation, and shrinkage of peat layers from the drainage networks and the extreme climate, the 2015 fires destroyed them, therefore leading to faster subsidence.

Unavailability of the data file of ground geodetic surveys limits our results of subsidence analysis to be more quantitatively validated. In addition, more field data and laboratory experiment are however needed to more quantitative and comprehensive analyze each factor and component influencing peatland subsidence.

The analysis of vegetation cover changes also demonstrates the impact of the 2015 fire. These results showed that their land cover changes are correlated with hotspot distributions, and the most severe degradation of vegetation cover (41%) occurred in October 2015. However, there was a trend of vegetation re-growth for post-fire. This post-fire vegetation re-growth indicates the potential of vegetation succession for carbon storage and regeneration.

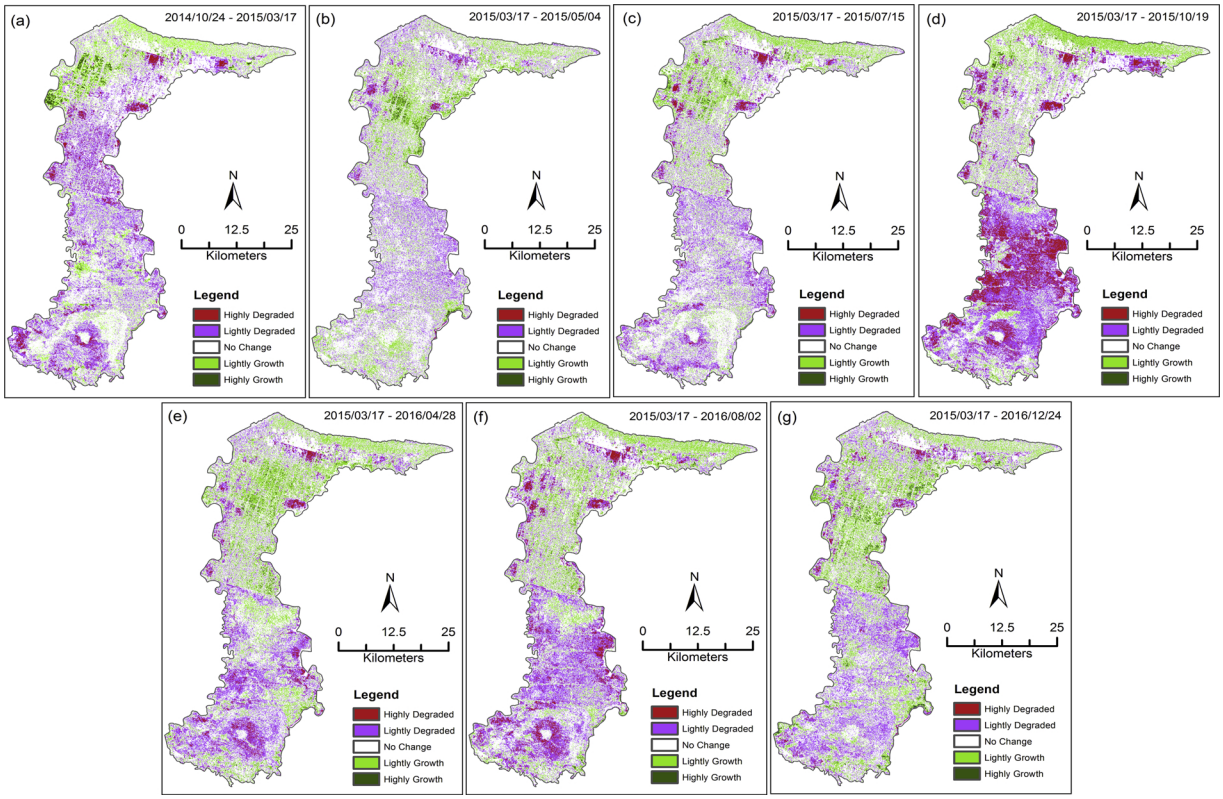

Fig. 11. Vegetation changes from 24 October 2014 to 24 December 2016 with the baseline of 17 March 2015.

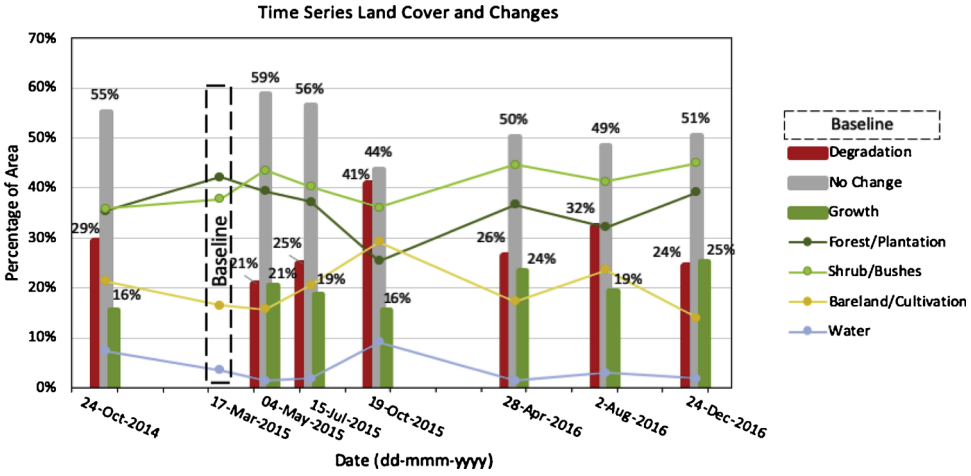

Fig. 12. Trends of percentage of each land cover types and of land cover changes.

Acknowledgement

We would like to acknowledge Sriwijaya University and the Ministry of Research, Technology and Higher Education of the Republic of Indonesia for their supports. We also thank the European Space Agency (ESA) for providing Sentinel-1 data and the SNAP software.

References

Abdikan, S., Sanli, F.B., Ustuner, M., Calò, F., 2016. Land cover mapping using sentinel-1 SAR data. Int. Arch. Photogramm. Remote Sens. Spat. Inf. Sci. - ISPRS Arch. 41, 757–761. https://doi.org/10.5194/isprsarchives-XLI-B7-757-2016.

Berardino, P., Lanari, R., Sansosti, E., 2002. A new algorithm for surface deformation monitoring based on small baseline differential SAR interferograms. IEEE Trans. Geosci. Remote Sens. 40, 2375–2383. https://doi.org/10.1109/TGRS.2002.803792.

BRG, 2017. Data Acquisition and Thematic Mapping in KHG Area.

Chen, C.W., Zebker, H.A., 2001. Of statistical models for cost functions in nonlinear optimization. J. Opt. Soc. Am. A 18, 338–351.

Congalton, R.G., 1991. A review of assessing the accuracy of classifications of remotely sensed data. Remote Sens. Environ. 37, 35–46. https://doi.org/10.1016/0034-4257(91)90048-B.

Couwenberg, J., Hooijer, A., 2013. Towards robust subsidence-based soil carbon emission factors for peat soils in south-east Asia, with special reference to oil palm plantations. Mires Peat 12, 1–13.

Deverel, S.J., Leighton, D.A., 2010. San Francisco Estuary and Watershed Science Historic, Recent, and Future Subsidence, Sacramento-San Joaquin Delta, California, USA. San Fr. Estuary Watershed Sci. 8, 1–24.

Gambolati, G., Putti, M., Teatini, P., Camporese, M., Ferraris, S., Gasparetto Stori, G., Nicoletti, V., Silvestri, S., Rizzetto, F., Tosi, L., 2005a. Peat land oxidation enhances subsidence in the venice watershed 86. Eos, Washington. DC), pp. 10–13. https://doi.org/10.1029/2005EO230001.

Gambolati, G., Putti, M., Teatini, P., Camporese, M., Ferraris, S., Gasparetto Stori, G., Nicoletti, V., Silvestri, S., Rizzetto, F., Tosi, L., 2005b. Peat Land Oxidation Enhances Subsidence in the Venice Watershed. Eos, Washington. DC), pp. 86. https://doi.org/10.1029/2005EO230001.

Geudtner, D., Torres, R., Snoeij, P., Ostergaard, A., Navas-Traver, I., 2013. Sentinel-1

mission capabilities and SAR system calibration. IEEE natl. Radar Conf. - Proc. 0–3. https://doi.org/10.1109/RADAR.2013.6586141.
Geudtner, D., Prats-Iraola, P., Shau, R., Bamler, R., Rodriguez Gonzalez, F., Yague-Martinez, N., Brcic, R., Eineder, M., 2016. Interferometric processing of Sentinel-1 TOPS data. IEEE Trans. Geosci. Remote Sens. 54, 2220–2234. https://doi.org/10.1109/tgrs.2015.2497902.
Goldstein, R.M., Werner, C.L., 1998. Radar interferogram filtering for geophysical applications. Geophys. Res. Lett. 25, 4035–4038. https://doi.org/10.1029/1998GL900033.
Grzywna, A., 2017. The degree of peatland subsidence resulting from drainage of land. Environ. Earth Sci. 76, 1–8. https://doi.org/10.1007/s12665-017-6869-1.
Hooijer, A., Page, S., Canadell, J.G., Silvius, M., Kwadijk, J., Wösten, H., Jauhiainen, J., 2010. Current and future CO 2 emissions from drained peatlands in Southeast Asia. Biogeosciences 7, 1505–1514. https://doi.org/10.5194/bg-7-1505-2010.
Hooijer, A., Page, S., Jauhiainen, J., Lee, W.A., Lu, X.X., Idris, A., Anshari, G., 2012a. Subsidence and carbon loss in drained tropical peatlands. Biogeosciences 9, 1053–1071. https://doi.org/10.5194/bg-9-1053-2012.
Hooijer, A., Triadi, B., Karyanto, O., Page, S.E., van der Vat, M., Erkens, G., 2012b. Subsidence in drained coastal peatland in SE Asian : implications for sustainability. Proceedings of the 14th International Peat Congress 1–8.
Hooijer, A., Page, S., Navratil, P., Vernimmen, R., Mawdsley, N., 2014. Carbon emissions from drained and Degraded Peatland in Indonesia and emission factors for measurement, reporting and verification (MRV) of peatland greenhouse gas emissions. Forda-Mof.Org 50.
Hotchinson, J.N., 1980. The rocord of peat wastage in the east anglian fenlands at holme post. J. Ecol. 68, 229–249. https://doi.org/10.2307/2259253.
Khakim, M.Y.N., Tsuji, T., Matsuoka, T., 2013. Detection of localized surface uplift by differential SAR interferometry at the hangingstone oil sand field, Alberta, Canada. IEEE J. Sel. Top. Appl. Earth Obs. Remote Sens. 6, 2344–2354. https://doi.org/10.1109/JSTARS.2013.2254471.
Khakim, M.Y.N., Tsuji, T., Matsuoka, T., 2014. Lithology-controlled subsidence and seasonal aquifer response in the Bandung basin, Indonesia, observed by synthetic aperture radar interferometry. Int. J. Appl. Earth Obs. Geoinf. 32, 199–207. https://doi.org/10.1016/j.jag.2014.04.012.
Kwoun, O.I., Lu, Z., Neal, C., Wicks, C., 2006. Quiescent deformation of the Aniakchak Caldera, Alaska mapped by InSAR. Geology 34, 5–8. https://doi.org/10.1130/G22015.1.
Limin, S.H., Yunsiska, E., Kitso, K., Alim, S., 2008. Restoration of hydrological status as the key to rehabilitation of demaged peatland in Central Kalimantan. Restoration of tropical peatlands. ALTERRA - Wageningen University and Research Centre, and the EU - RESTORPEAT Partnership, the Netherlands, pp. 118–124.
Murdiyarso, D., Dewi, S., Lawrence, D., Seymour, F., 2011. Indonesia's Forest Moratorium: a Stepping Stone to Better Forest Governance? CIFOR, Bogor, Indonesia. https://doi.org/10.17528/cifor/003561.
Page, S.E., Siegert, F., Rieley, J.O., Boehm, H.V., Jaya, A., Limin, S., 2002. The amount of carbon released from peat and forest fires in Indonesia during 1997 Susan. Nature 420, 61–65. https://doi.org/10.1038/nature01141.1.
Prats-Iraola, P., Scheiber, R., Marotti, L., Wollstadt, S., Reigber, A., 2012. TOPS interferometry with terraSAR-X. IEEE Trans. Geosci. Remote Sens. 50, 3179–3188. https://doi.org/10.1109/TGRS.2011.2178247.
Roy, P.D., Rivero-Navarrete, A., Sánchez-Zavala, J.L., López-Balbiaux, N., 2014. Subsurface fire and subsidence at Valle del Potosí (Nuevo León, Mexico): preliminary observations. Bol. la Soc. Geol. Mex. 66, 553–557. https://doi.org/10.18268/BSGM2014v66n3a10.
Samsonov, S., van der Kooij, M., Tiampo, K., 2011. A simultaneous inversion for deformation rates and topographic errors of DInSAR data utilizing linear least square inversion technique. Comput. Geosci. 37, 1083–1091. https://doi.org/10.1016/j.cageo.2011.01.007.
Shimada, M., Watanabe, M., Motooka, T., 2013. Subsidence estimation of the peatland forest in the central Kalimantan using the PALSAR time series differential interferometry. Int. Geosci. Remote Sens. Symp. 1846–1849. https://doi.org/10.1109/IGARSS.2013.6723161.
Stephens, J.C., 1956. Subsidence of organic soils in the Florida everglades1. Soil Sci. Soc. Am. J. 20, 77. https://doi.org/10.2136/sssaj1956.03615995002000010019x.
Story, M., Congalton, R.G., 1986. Remote sensing brief accuracy assessment: a user's perspective. Photogramm. Eng. Remote Sensing 52, 397–399.
Wang, X., Ge, L., Li, X., 2012. Evaluation of filters for envisat asar speckle suppression in pasture area. ISPRS Ann. Photogramm. Remote Sens. Spat. Inf. Sci. I–7, 341–346. https://doi.org/10.5194/isprsannals-I-7-341-2012.
Wosten, J.H., Ismail, A., van Wijk, A.L.M., 1997. Peat subsidence and its practical implications: a case study in Malaysia. Geoderma 78, 25–36. https://doi.org/10.1016/S0016-7061(97)00013-X.
Yu, C., Li, Z., Penna, N.T., 2018a. Interferometric synthetic aperture radar atmospheric correction using a GPS-based iterative tropospheric decomposition model. Remote Sens. Environ. 204, 109–121. https://doi.org/10.1016/j.rse.2017.10.038.
Yu, C., Li, Z., Penna, N.T., Crippa, P., 2018b. Generic atmospheric correction model for interferometric synthetic aperture radar observations. J. Geophys. Res. Solid Earth 123, 9202–9222. https://doi.org/10.1029/2017JB015305.
Zhou, Z., Li, Z., Waldron, S., Tanaka, A., 2016. Monitoring Peat subsidence and carbon emission in Indonesia peatlands using INSAR time series. International Geoscience and Remote Sensing Symposium (IGARSS) 6797–6798. https://doi.org/10.1109/IGARSS.2016.7730774.